

Observing localisation in a 2D quasicrystalline optical lattice

Matteo Sbroscia,^{1,*} Konrad Viebahn,^{1,2} Edward Carter,¹
 Jr-Chiun Yu,¹ Alexander Gaunt,³ and Ulrich Schneider^{1,†}

¹*Cavendish Laboratory, University of Cambridge,
 J. J. Thomson Avenue, Cambridge CB3 0HE, United Kingdom*

²*Institute for Quantum Electronics, ETH Zürich, 8093 Zürich, Switzerland*

³*DeepMind, 6 Pancras Square, London N1C 4AG, United Kingdom*

(Dated: January 30, 2020)

Quasicrystals are long-range ordered but not periodic, representing an interesting middle ground between order and disorder. We experimentally and numerically study the ground state of non- and weakly-interacting bosons in an eightfold symmetric quasicrystalline optical lattice. We find extended states for weak lattices but observe a localisation transition at a lattice depth of $V_0 = 1.78(2) E_{\text{rec}}$ for the non-interacting system. We identify this transition by measuring the timescale required for adiabatic loading into the lattice, which diverges at the critical lattice depth for localisation. Gross-Pitaevskii simulations show that in interacting systems the transition is shifted to deeper lattices, as expected from superfluid order counteracting localisation. Our experimental results are consistent with such a mean-field shift. Quasiperiodic potentials, lacking conventional rare regions, provide the ideal testing ground to realise many-body localisation in 2D.

Quasiperiodic potentials give rise to fractal, self-similar structures both in momentum space [1] and in their energy spectrum [2]. The unique and intriguing status of quasiperiodicity as a middle ground between order and disorder has generated interests in a wide range of fields, from recent experiments with twisted bilayer graphene [3], topological photonics [4], and ultracold atoms [5–9], to a proof for the undecidability of the spectral gap theorem [10]. Combining two-dimensional (2D) quasicrystalline potentials with ultracold atoms will not only enable the observation of the 2D Bose glass [11, 12] but could prove essential for deciding the ultimate fate of many-body localisation (MBL) in 2D. Though established and confirmed in 1D [8, 13], the existence of MBL in higher dimensions is — despite first experimental studies [14, 15] — less clear, as rare ergodic enclosures might trigger a thermalisation avalanche that destabilises the localised state [16, 17]. In quasiperiodic systems, in contrast, the long-range ordered nature of the potential precludes such conventional rare ergodic regions [18].

By studying the diverging timescale required for adiabatically loading a Bose-Einstein condensate (BEC) of $\sim 3 \times 10^5$ ^{39}K atoms into a quasicrystalline optical lattice, we probe the disorder-induced localised phase and its resilience against interactions. We perform the investigation in momentum space by recording matterwave diffraction patterns, instead of employing the real space in-situ techniques mostly used so far. We create a quasicrystalline 2D optical lattice $V(\mathbf{r})$ by superimposing four coplanar 1D lattices formed by retro-reflected laser beams (wavelength $\lambda_{\text{lat}} = 725$ nm) under 45° angles and mutually detuned by at least 10 MHz, as illustrated in Fig. 1a:

$$V(\mathbf{r}) = V_0 \sum_{i=1}^4 \sin^2(\mathbf{k}_i \cdot \mathbf{r}), \quad (1)$$

$$\mathbf{k}_i \in \frac{2\pi}{\lambda_{\text{lat}}} \cdot \left\{ \begin{pmatrix} 1 \\ 0 \end{pmatrix}, \frac{1}{\sqrt{2}} \begin{pmatrix} \pm 1 \\ 1 \end{pmatrix}, \begin{pmatrix} 0 \\ 1 \end{pmatrix} \right\}. \quad (2)$$

Analogously to solid-state quasicrystals [19] this potential exhibits a crystallographically forbidden eightfold rotational symmetry [20]. Fig. 1b shows the numerically calculated single-particle ground state of this potential for different lattice depths V_0 . In contrast to periodic lattices, there exists a critical lattice strength V_{loc} at which the ground state undergoes a transition from an extended, quasiperiodic Bloch wave to an exponentially localised state. The quasiperiodic potential generically possesses a *single* absolute minimum and the absolute ground state in the localised phase is centred around this site.

Since disorder-induced localised phases cannot be detected in equilibrium, we rely on a dynamical probe: starting with a non-interacting BEC in a dipole trap (see [20] for details), we increase the lattice depth linearly from 0 to V_0 in a time τ before decreasing it back to 0 using the same ramp and performing time-of-flight imaging, as illustrated in Fig. 1c. Whenever the loading and unloading dynamics under this triangular ramp are fully adiabatic, all atoms return to the initial BEC wavefunction and we detect them all at zero momentum.

For $V_0 < V_{\text{loc}}$, the lattice ground state is a quasiperiodic but extended wave (Fig. 1b) and the initially constant density only has to rearrange locally. Similarly to a periodic lattice [22] (discussed later), the BEC can hence be adiabatically loaded in a finite time. Above the localisation transition at V_{loc} , on the other hand, the initially extended ground state wavefunction becomes exponentially localised around the typically unique global minimum and is characterised by a rapidly shrinking localisation length. Following this change adi-

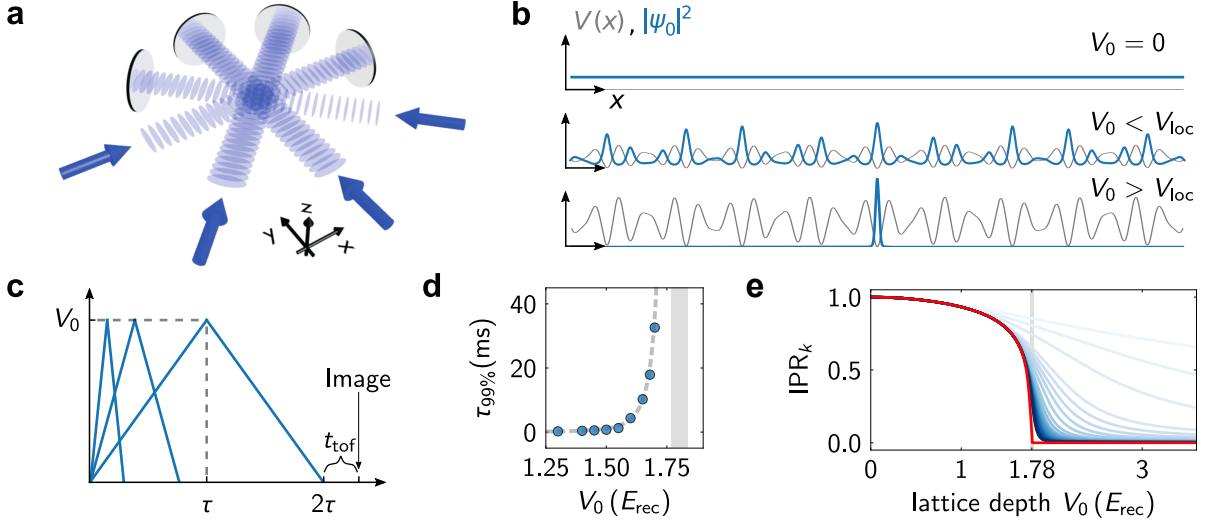


Fig. 1 | Localisation in a 2D quasicrystalline optical lattice. **a**, Eightfold symmetric quasicrystalline optical lattice formed by superimposing four standing waves. **b**, Numerically computed single-particle ground states for lattice depths below ($V_0/E_{\text{rec}} = 0, 1$) and above ($V_0/E_{\text{rec}} = 2$) the localisation transition. Grey lines denote the lattice potential. **c**, The lattice ramp used in all experiments. The final momentum distribution is detected using a time-of-flight of $t_{\text{tof}} = 33$ ms. **d**, Numerically calculated ramp time (circles) needed for a 99% recovery of the zero-momentum peak population in the quasicrystalline lattice. This timescale diverges at a lattice depth (grey bar) compatible with the localisation transition (V_{loc}). The dashed line denotes a phenomenological fit [21]. **e**, Calculated Inverse Participation Ratio of the single-particle ground state in momentum space (IPR_k), exhibiting a cusp at the critical lattice depth $V_{\text{loc}} \approx 1.78(2) E_{\text{rec}}$ (grey bar). Darker blue lines correspond to larger basis sets; the red line marks the extrapolation to the infinite basis, see supplemental material [21].

abatically would require particle transport over large distances, leading to a diverging adiabatic-

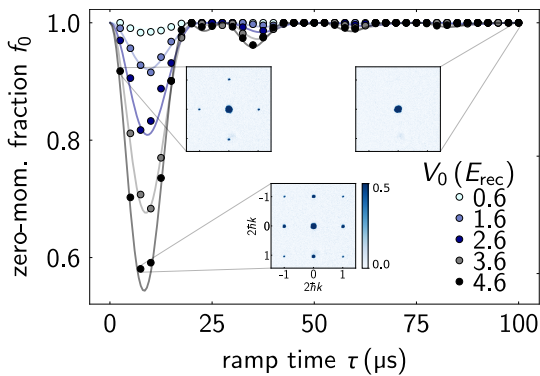


Fig. 2 | Adiabatic triangular lattice ramps for a regular square lattice. The zero-momentum fraction f_0 is fully recovered for all probed lattice depths already for rather short ramp durations of $\tau \gtrsim 40 \mu\text{s}$. Different colors correspond to different maximum lattice depths V_0 ; solid lines denote numerical solutions to the single-particle Schrödinger equation [21]. Insets show time-of-flight images for $V_0 = 4.6 E_{\text{rec}}$ and different ramp times τ : the optical density colorscale is chosen to highlight small excited populations, thereby saturating the zero-momentum peak.

ity timescale in the thermodynamic limit. This prediction is confirmed by the numerical simulation shown in Fig. 1d: the ramp time τ needed to return $> 99\%$ of the atoms to the zero-momentum state diverges upon approaching the localisation transition [21]. In order to precisely pinpoint the critical lattice depth, we numerically calculate the single-particle ground state using a plane wave basis and compute its Inverse Participation Ratio in momentum space $\text{IPR}_k = \sum_j |\tilde{\psi}_j|^4$, where $\tilde{\psi}_j$ denotes the amplitude of the j^{th} plane wave [21]. As shown in Fig. 1e, this displays a sharp transition at $V_{\text{loc}} = 1.78(2) E_{\text{rec}}$, which is consistent with a numerical calculation of the localisation transition in real space [23].

In our experiments, we first focus on non-interacting atoms (scattering length $a \approx 0 a_0$ [24]) and a regular square lattice generated by two of the four standing waves. In this periodic case there is no localisation transition and adiabatic loading should thus always be possible [22]. We individually fit all momentum peaks in the time-of-flight images taken at the end of the lattice ramp and extract both the total number of atoms N and the atom number in the zero-momentum peak N_0 . Hence we define $f_0 = N_0/N$ as the zero-momentum fraction, plotted in Fig. 2 as a function of the ramp time τ . For $\tau = 0$ the atoms have

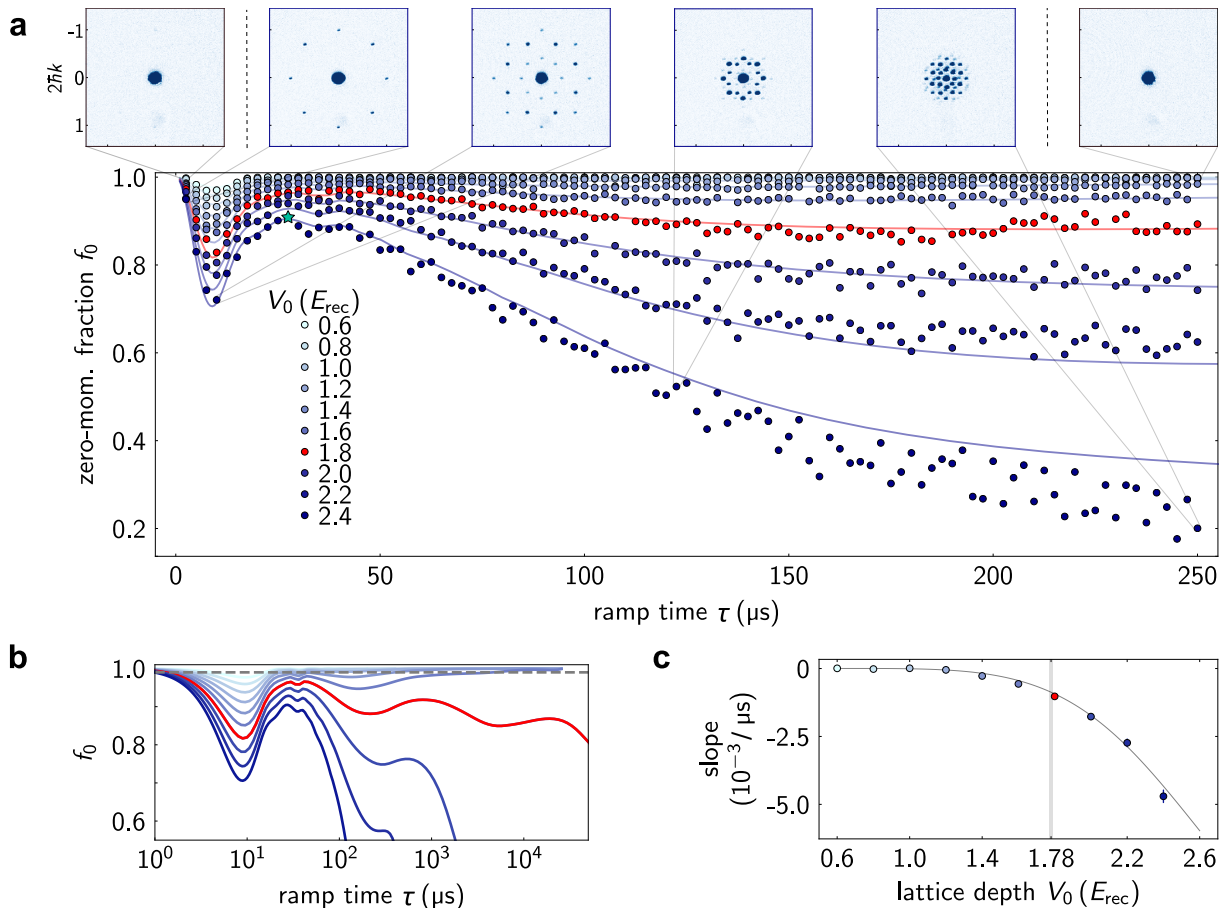


Fig. 3 | Breakdown of adiabaticity in a quasicrystalline lattice. **a**, Final population of the zero-momentum state for the quasicrystalline lattice. Solid lines denote the numerical solution to the single-particle Schrödinger equation [21], also shown in **b** for longer ramp times. Both experiment and simulation show that the zero-momentum fraction f_0 ultimately recovers to one for $V_0 < V_{\text{loc}}$, but tends to zero for $V_0 > V_{\text{loc}}$. The red data denotes the lowest probed lattice depth above the localisation transition, which is also the first one not to recover. The turquoise star denotes the maximum recovery for $2.4 E_{\text{rec}}$. The first and last insets in **a** show time-of-flight images for $0.6 E_{\text{rec}}$, all others are for $2.4 E_{\text{rec}}$; the colorscale is identical to Fig. 2. The dashed line in **b** denotes 99% recovery, the ramp time required to reach this is plotted in Fig. 1d. **c**, Fitted slopes for $\tau = 50 - 100 \mu\text{s}$: large negative slopes indicate localisation.

no time to respond and they simply remain in the zero-momentum state, hence $f_0 = 1$. For small but finite ramp times, which mean rather abrupt lattice changes, the non-adiabatic dynamics gives rise to significant excitations that are strongest for ramp times around $\tau \approx 10 \mu\text{s}$. For slower ramps, the atoms begin to adiabatically follow the ground state and return to the initial state, eventually leading to a full recovery of the zero-momentum peak population for all inspected lattice depths. The oscillatory behaviour at intermediate ramp times stems from only a few discrete momenta being relevant to the dynamics [20, 22]. Our observations are in perfect agreement with a numerical solution of the single-particle Schrödinger equation for a homogeneous lattice without any trap (solid lines in Fig. 2). The observed timescales for adiabatic loading ($< 100 \mu\text{s}$) are much shorter than

those typically used ($50 - 200 \text{ ms}$ [25]), as the system is non-interacting and we can neglect the harmonic trap on these short timescales [21].

In the quasicrystalline lattice, in contrast, the dynamics at long ramp times crucially depends on whether the maximum lattice depth lies below or above the localisation transition at $V_{\text{loc}} = 1.78(2) E_{\text{rec}}$. As shown in Fig. 3a, the dynamics starts similarly to the periodic case, also giving rise to a maximum depletion around $\tau \approx 10 \mu\text{s}$. For longer ramps, however, the quasiperiodic character leads to two dramatically distinct behaviours: while for low lattice depths the zero-momentum peak eventually fully recovers (see also Fig. 3b), it never does for $V_0 > V_{\text{loc}}$. Its population instead keeps decreasing and ultimately tends to zero for slower ramps, where atoms can reach higher diffraction orders. These include states at succes-

sively lower momenta and lead to the atoms “getting lost” in the fractal momentum space of the quasicrystal [20]. This is directly visible in the time-of-flight pictures at the top of Fig. 3a, where the populated momenta are situated closer to the origin for longer τ . A numerical solution of the single-particle Schrödinger equation (solid lines in Fig. 3a) not only agrees very well with the experimental data, but furthermore allows exploration of much slower ramps without trap effects (Fig. 3b), confirming the two distinct dynamics for slow ramps. All traces show log-periodic oscillations, which are a sign of discrete scale invariance and of the fractal nature of the system [26]. Fig. 3c shows the gradients extracted from linear fits between $\tau = 50 - 100 \mu\text{s}$. While the log-periodic oscillations can give rise to shallow negative slopes even below the transition, localisation causes stronger negative slopes that highlight the counterintuitive nature of the dynamics in this regime – the slower the ramps, the further away from adiabaticity. The small discrepancies at long ramp times are probably caused by slightly inaccurate lattice depth calibrations.

In order to investigate the effect of repulsive interactions on the localisation transition, we applied different magnetic fields during the lattice ramp to sample scattering lengths between $0 - 200 a_0$, as shown in Fig. 4. In this rather deep lattice of $V_0 = 2.4 E_{\text{rec}} > V_{\text{loc}}$ the non-interacting ground state is strongly localised, leading to a very low recovery of the zero-momentum fraction of $f_0 \approx 0.2$ for a ramp time $\tau = 250 \mu\text{s}$. Interestingly, adding sufficiently strong repulsive interactions increases the recovered fraction to almost unity. The dashed line at $f_0 \approx 0.9$ denotes the recovered fraction at its maximum value for $\tau \approx 30 \mu\text{s}$ (turquoise star in Fig. 3a), which is essentially independent of the interaction strength (see supplemental material [21]). For weak interactions, the low recovered fraction after $250 \mu\text{s}$ therefore directly corresponds to strong negative slopes that signal localisation, whereas the close to perfect recovery for larger interactions suggest that no phase transition has been crossed. This is consistent with the expectation that repulsive interactions in a BEC shift the onset of localisation to deeper lattices. The same effect can also be observed in the Gross-Pitaevskii equation (GPE) simulations [21] shown in the main inset of Fig. 4, where the superfluid fraction ψ_{SF} vanishes only at deeper lattices in the interacting case.

By recording matterwave diffraction patterns after a triangular lattice ramp, we could observe the localisation transition in a 2D quasiperiodic potential, thereby establishing a novel and complementary observable to study disorder-induced localisation. The timescale required for adiabatic

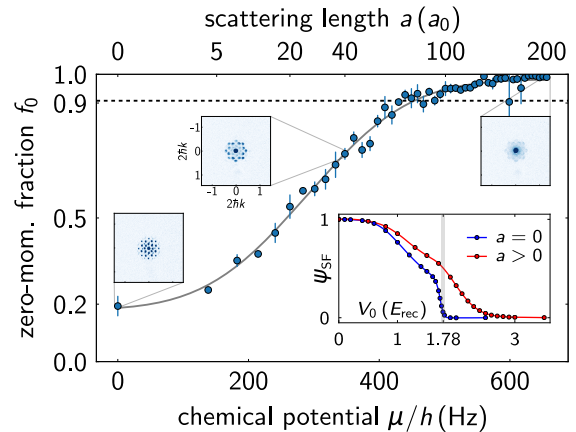


Fig. 4 | Effect of repulsive interactions. The zero-momentum fraction for a fixed slow ramp $\tau = 250 \mu\text{s}$ and deep lattice $V_0 = 2.4 E_{\text{rec}}$ increases with growing interaction strengths, given by the scattering length (a) and the resulting chemical potential ($\mu \propto a^{2/5}$). The black solid line denotes a phenomenological fit using the error function of equation (18) in [21]. Error bars denote the standard deviation of three measurements. The main inset is a mean-field GPE simulation of the superfluid stiffness or fraction ψ_{SF} [21] showing that the localisation transition is pushed to deeper lattices in interacting systems. The colorscale used in the small insets is identical to Fig. 2. The chemical potential scale has a systematic uncertainty on the order of 10–15% stemming from the atom number calibration.

ically loading a non-interacting condensate into the lattice diverges at the localisation transition at $V_{\text{loc}} \approx 1.78(2) E_{\text{rec}}$, as the change from an extended to a localised wavefunction would require mass transport across the whole system. The localised phase is stable against adding small repulsive interactions and the observed behaviour is consistent with a mean-field shift of the transition point. Adding a strong 1D lattice along the third direction will extend these experiments into the 2D regime and allow for strong correlations. This will provide access to the full disorder versus interaction phase diagram, including the so far elusive 2D Bose glass and a re-entrant transition where adding disorder turns a Mott insulator back into a superfluid [12]. Localised states in 2D quasiperiodic potentials could prove crucial for studying MBL in 2D, as their long-range ordered nature ensures that conventional rare ergodic regions are absent [18]. They are also an ideal starting point to study interacting Floquet systems, where the non-ergodicity could effectively mitigate the typical Floquet heating [27, 28].

ACKNOWLEDGEMENTS

We would like to thank Oliver Brix, Michael Höse, Max Melchner, and Hendrik von Raven for assistance during the construction of the experiment, and Shaurya Bhawe for assistance in the final stages of the measurements. We are grateful to Zoran Hadzibabic and his team, Juan Garrahan, and Attila Szabó for helpful discussions. This work was partly funded by the European Commission ERC Starting Grant QUASICRYSTAL, the EPSRC Grant (EP/R044627/1), and Programme Grant DesOEQ (EP/P009565/1).

* current address: Jet Propulsion Laboratory, California Institute of Technology, 4800 Oak Grove Drive, Pasadena, CA, 91109, USA

† uws20@cam.ac.uk

- [1] Marjorie Senechal, *Quasicrystals and geometry* (Cambridge University Press, Cambridge, 1995).
- [2] Joaquim Puig, “Cantor Spectrum for Quasi-Periodic Schrödinger Operators,” in *Mathematical Physics of Quantum Mechanics*, Vol. 690, edited by Joachim Asch and Alain Joye (Springer Berlin Heidelberg, 2006) pp. 79–91.
- [3] Sung Joon Ahn, Pilkyung Moon, Tae-Hoon Kim, Hyun-Woo Kim, Ha-Chul Shin, Eun Hye Kim, Hyun Woo Cha, Se-Jong Kahng, Philip Kim, Mikito Koshino, Young-Woo Son, Cheol-Woong Yang, and Joung Real Ahn, “Dirac electrons in a dodecagonal graphene quasicrystal,” *Science* **361**, 782–786 (2018).
- [4] Z. Vally Vardeny, Ajay Nahata, and Amit Agrawal, “Optics of photonic quasicrystals,” *Nature Photonics* **7**, 177 (2013).
- [5] L. Guidoni, C. Triché, P. Verkerk, and G. Grynberg, “Quasiperiodic Optical Lattices,” *Phys. Rev. Lett.* **79**, 3363–3366 (1997).
- [6] Giacomo Roati, Chiara D’Errico, Leonardo Fallani, Marco Fattori, Chiara Fort, Matteo Zaccanti, Giovanni Modugno, Michele Modugno, and Massimo Inguscio, “Anderson localization of a non-interacting Bose–Einstein condensate,” *Nature* **453**, 895–898 (2008).
- [7] Bryce Gadow, Daniel Pertot, Jeremy Reeves, Matthias Vogt, and Dominik Schneble, “Glassy behavior in a binary atomic mixture,” *Physical Review Letters* **107**, 145306 (2011).
- [8] M. Schreiber, S. S. Hodgman, P. Bordia, H. P. Lüschen, M. H. Fischer, R. Vosk, E. Altman, U. Schneider, and I. Bloch, “Observation of many-body localization of interacting fermions in a quasirandom optical lattice,” *Science* **349**, 842–845 (2015).
- [9] Shankari V. Rajagopal, Toshihiko Shimasaki, Peter Dotti, Mantas Račiūnas, Ruwan Senaratne, Egidijus Anisimovas, André Eckardt, and David M. Weld, “Phasonic Spectroscopy of a Quantum Gas in a Quasicrystalline Lattice,” *Physical Review Letters* **123**, 223201 (2019).
- [10] Toby S. Cubitt, David Perez-Garcia, and Michael M. Wolf, “Undecidability of the spectral gap,” *Nature* **528**, 207 (2015).
- [11] Matthew P. A. Fisher, Peter B. Weichman, G. Grinstein, and Daniel S. Fisher, “Boson localization and the superfluid-insulator transition,” *Phys. Rev. B* **40**, 546–570 (1989).
- [12] S Söyler, M. Kiselev, N. V. Prokofev, and B. V. Svistunov, “Phase Diagram of the Commensurate Two-Dimensional Disordered Bose-Hubbard Model,” *Phys. Rev. Lett.* **107**, 185301 (2011).
- [13] Jens H. Bardarson, Frank Pollmann, Ulrich Schneider, and Shivaji Sondhi, “Special issue: Many-body localization,” *Annalen der Physik* **529** (2017).
- [14] Jae-yoon Choi, Sebastian Hild, Johannes Zeiher, Peter Schauß, Antonio Rubio-Abadal, Tarik Yefsah, Vedika Khemani, David A. Huse, Immanuel Bloch, and Christian Gross, “Exploring the many-body localization transition in two dimensions,” *Science* **352**, 1547–1552 (2016).
- [15] Pranjal Bordia, Henrik Lüschen, Sebastian Scherg, Sarang Gopalakrishnan, Michael Knap, Ulrich Schneider, and Immanuel Bloch, “Probing slow relaxation and many-body localization in two-dimensional quasiperiodic systems,” *Phys. Rev. X* **7**, 041047 (2017).
- [16] Wojciech De Roeck and François Huveneers, “Stability and instability towards delocalization in many-body localization systems,” *Phys. Rev. B* **95**, 155129 (2017).
- [17] Ionut Dragos Potirniche, Sumilan Banerjee, and Ehud Altman, “Exploration of the stability of many-body localization in $d > 1$,” *Physical Review B* **99** (2019).
- [18] Attila Szabó and Ulrich Schneider, “Mixed spectra and partially extended states in a two-dimensional quasiperiodic model,” *Physical Review B* **101**, 014205 (2020).
- [19] D. Shechtman, I. Blech, D. Gratias, and J. W. Cahn, “Metallic Phase with Long-Range Orientational Order and No Translational Symmetry,” *Phys. Rev. Lett.* **53**, 1951–1953 (1984).
- [20] Konrad Viebahn, Matteo Sbroscia, Edward Carter, Jr-Chium Yu, and Ulrich Schneider, “Matter-Wave Diffraction from a Quasicrystalline Optical Lattice,” *Phys. Rev. Lett.* **122**, 110404 (2019).
- [21] See supplemental material.
- [22] J. Hecker Denschlag, J. E. Simsarian, H. Häffner, C. McKenzie, A. Browaeys, D. Cho, K. Helmerston, S. L. Rolston, and W. D. Phillips, “A Bose-Einstein condensate in an optical lattice,” *Journal of Physics B: Atomic, Molecular and Optical Physics* **35**, 3095–3110 (2002).
- [23] Attila Szabó and Ulrich Schneider, “Non-power-law universality in one-dimensional quasicrystals,” *Phys. Rev. B* **98**, 134201 (2018).
- [24] Richard J. Fletcher, Raphael Lopes, Jay Man, Nir Navon, Robert P. Smith, Martin W. Zwierlein, and Zoran Hadzibabic, “Two- and three-body contacts in the unitary Bose gas,” *Science* **355**, 377–380 (2017).
- [25] T. Gericke, F. Gerbier, A. Widera, S. Fölling, O. Mandel, and I. Bloch, “Adiabatic loading of a Bose–Einstein condensate in a 3D optical lattice,”

- Journal of Modern Optics **54**, 735–743 (2007).
- [26] Didier Sornette, “Discrete-scale invariance and complex dimensions,” *Physics Reports* **297**, 239 – 270 (1998).
 - [27] André Eckardt, “Colloquium: Atomic quantum gases in periodically driven optical lattices,” *Reviews of Modern Physics* **89** (2017).
 - [28] Pranjali Bordia, Henrik Lüschen, Ulrich Schneider, Michael Knap, and Immanuel Bloch, “Periodically driving a many-body localized quantum system,” *Nature Physics* **13**, 460 (2017).
 - [29] Tomoki Ozawa and Hannah M. Price, “Topological quantum matter in synthetic dimensions,” *Nature Reviews Physics* **1**, 349–357 (2019).
 - [30] A.L. Gaunt, *Degenerate Bose Gases: Tuning Interactions & Geometry* (University of Cambridge, 2015) PhD thesis.
 - [31] Elliott H. Lieb, Robert Seiringer, and Jakob Yngvason, “Superfluidity in dilute trapped Bose gases,” *Physical Review B* **66** (2002).
 - [32] L. P. Pitaevskii, S. Stringari, *Bose-Einstein condensation and superfluidity* (Oxford University Press, Oxford, 2016).

SUPPLEMENTAL MATERIAL

Experimental details

The experimental apparatus and sequence is described in the supplemental material of [20]. We load $2.5 - 3 \times 10^5$ ^{39}K BEC atoms from a $(\omega_x, \omega_y, \omega_z) = 2\pi \cdot (19, 18, 115)$ Hz crossed-beam dipole trap into a $\lambda_{\text{lat}} = 725$ nm blue-detuned lattice in the x, y -plane. In order to avoid interferences between the individual 45° -spaced 1D lattices, they are detuned from each other by at least 10 MHz, much higher than any frequency the atoms could respond to. There is no lattice along the third direction.

All images are taken after a 33 ms time-of-flight, and 2 ms into it interactions are re-introduced to a value of $a = 280 a_0$ in order to “puff up” the diffraction orders and to minimise saturation of the images, which would otherwise prevent a reliable fitting procedure. The lack of visible scattering spheres in the images demonstrates that the effects of the “puffing up” on the dynamics is negligible.

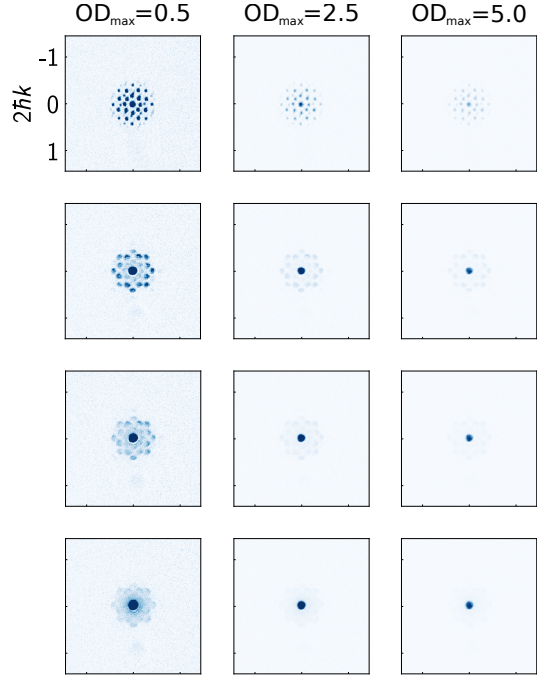
We can neglect the effects of the harmonic trap, as they would start to dominate only after times on the order of $1/\omega_{x,y} \approx 10$ ms.

Population extraction

The populations of the individual momenta are extracted by fitting a Thomas-Fermi profile to each peak independently. A fit is performed instead of a pixel count as it allows for a reliable characterisation of the peaks even in the presence of noise and (more importantly) saturation. Despite the “puffing up” procedure, the zero-momentum peak (the original BEC) remains almost always severely saturated. Only points below a cutoff of $\text{OD} = 3.4$ are considered in the fit, OD being the optical density.

For higher diffraction orders, the fits are generally reliable for the square and for the short-term dynamics of the eightfold quasiperiodic lattices, where the peaks are well separated. For the longest and deepest quasiperiodic lattice ramps, on the other hand, atoms start to occupy up to the 10th diffraction order, such that peaks begin to overlap in the images.

The color scale chosen for all insets presented in the paper was capped at $\text{OD} = 0.5$ in order to emphasise small excited populations. This choice in turn visually over-emphasises the spatial extent and hence the population of the zero-momentum peak, which in the deeply localised regions is highly depleted. As shown in Extended Data Fig. 1, different colorscales visually confirm that higher interaction strengths result in an almost complete recovery of the zero-momentum peak.



Extended Data Fig. 1 | Different colorscales. The four different rows, starting from the top one, correspond to $a/a_0 = 0, 40, 100,$ and 200 .

Simulations

Momentum space

The numerical data presented in Fig. 1e and Fig. 2 was produced by solving the single-particle problem using a momentum space representation. As the four 1D lattices (depicted in Fig. 1a) are detuned from each other by at least 10 MHz, there is no relevant cross interference and the main interaction consists of atoms absorbing a photon from one laser beam and remitting it into the counter-propagating beam. This changes the atomic momentum by $2\hbar\mathbf{k}$. The wavevectors of the four incoming beams have the same magnitude $|\mathbf{k}| = 2\pi/\lambda_{\text{lat}}$ and only differ in their direction, as listed in equation (2).

Employing the language of synthetic dimensions [29], the four 2D wavevectors can be chosen as orthogonal vectors in a four dimensional space:

$$\mathbf{k}_1 = \begin{pmatrix} 1 \\ 0 \end{pmatrix} \rightarrow \begin{pmatrix} 1 \\ 0 \\ 0 \\ 0 \end{pmatrix}, \quad \mathbf{k}_2 = \frac{1}{\sqrt{2}} \begin{pmatrix} 1 \\ 1 \end{pmatrix} \rightarrow \begin{pmatrix} 0 \\ 1 \\ 0 \\ 0 \end{pmatrix}, \quad (3)$$

$$\mathbf{k}_3 = \frac{1}{\sqrt{2}} \begin{pmatrix} -1 \\ 1 \end{pmatrix} \rightarrow \begin{pmatrix} 0 \\ 0 \\ 1 \\ 0 \end{pmatrix}, \quad \mathbf{k}_4 = \begin{pmatrix} 0 \\ 1 \end{pmatrix} \rightarrow \begin{pmatrix} 0 \\ 0 \\ 0 \\ 1 \end{pmatrix}, \quad (4)$$

where the common factor $2\pi/\lambda_{\text{lat}}$ has been omitted.

Starting from a zero-momentum state ($\mathbf{q} = 0$), the atoms can then reach the following momenta \mathbf{b}_p (matterwave diffraction vectors) by two-photon transitions:

$$\mathbf{b}_p/2 = i\mathbf{k}_1 + j\mathbf{k}_2 + \ell\mathbf{k}_3 + m\mathbf{k}_4, \quad (i, j, \ell, m) \in \mathbb{Z}^4. \quad (5)$$

Each coefficient represents the number of two-photon transitions along one of the standing waves (1D lattices). The blue lines in Fig. 1e correspond to the following truncations:

$$|i| + |j| + |\ell| + |m| \leq n \quad \text{for } n = 1 - 25. \quad (6)$$

The single-particle d -dimensional Hamiltonian for $\mathbf{q} = 0$, where d is the number of active lattice beams and hence the dimensionality of the augmented space, is then given by:

$$H_{p,q}^d(t) = \begin{cases} E_{\text{rec}} \times |\mathcal{P}_d^\parallel \cdot \mathbf{b}_p|^2 + d\frac{V_0(t)}{2} & \text{for } p = q \\ V_0(t)/4 & \text{for } ||p - q|| = 1 \\ 0 & \text{otherwise,} \end{cases} \quad (7)$$

where \mathbf{b}_p is the basis vector of equation (5) with $p = (i, j, \ell, k)$ and \mathcal{P}^\parallel is the projection matrix from the augmented back to the physical 2D basis. For the regular square lattice $d = 2$, while for the eight-fold quasicrystalline lattice $d = 4$, and the projection matrix \mathcal{P}_4^\parallel is

$$\mathcal{P}_4^\parallel = \begin{pmatrix} 1 & \cos \pi/4 & -\cos \pi/4 & 0 \\ 0 & \sin \pi/4 & \sin \pi/4 & 1 \\ 0 & 0 & 0 & 0 \\ 0 & 0 & 0 & 0 \end{pmatrix}. \quad (8)$$

We determine the ground state of H using Lanczos' algorithm and calculate the ground state IPR_k shown in Fig. 1e.

The dynamical simulations of Fig. 2 were obtained by direct integration of the dimensionless Schrödinger equation:

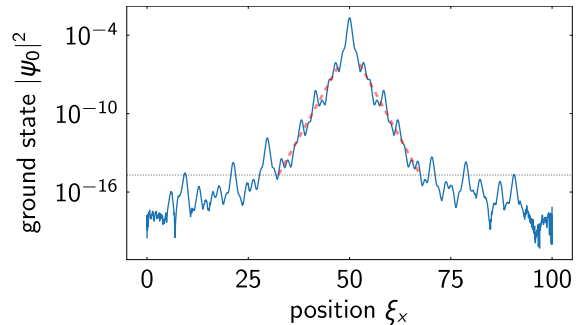
$$i \frac{d}{d\tau_{\text{rec}}} |\psi\rangle = H' |\psi\rangle, \quad (9)$$

where $H' = H/E_{\text{rec}}$ and $\tau_{\text{rec}} = \hbar/E_{\text{rec}}$.

The simulation requires a truncation in the plane wave basis, which limits the reliability of its predicted dynamics near the localisation transition because of the large number of Fourier components involved. Hence, a real space simulation was employed in these regions (next section).

Real space

The numerical data in Fig. 1b, Fig. 1d, Fig. 3, and in the inset of Fig. 4 was produced using the



Extended Data Fig. 2 | Exponentially decaying wavefunction in the localised state. The GPE of equation (10) was evolved in imaginary time for $\alpha = 2$ to find the (localised) ground state, whose density profile $|\psi_0|^2$ is plotted here as a function of the dimensionless coordinate ξ_x . The red dashed lines show the characteristic exponential localisation around the global minimum (chosen to lie at $\xi_x = 50$ here). The dashed grey line denotes where the simulation stops being reliable due to float precision and finite evolution time, signalled by the loss of even symmetry.

dimensionless Gross-Pitaevskii equation (GPE) in real space. It was solved using the split-step Fourier method [30] in the presence of an external potential energy term:

$$i \frac{\partial \psi'}{\partial \tau_{\text{rec}}} = -\nabla_{\xi}^2 \psi' + \alpha V(\xi) \psi' + 8\pi a' |\psi'|^2 \psi', \quad (10)$$

with $\xi = k_{\text{lat}} \mathbf{x}$, $a' = ak_{\text{lat}}$ and $\psi' = \psi/k_{\text{lat}}^{3/2}$. The lattice depth in units of E_{rec} is α . The non-interacting (single-particle) case was realised by setting $a' = 0$. The use of this mean-field calculation is further justified by the absence of an additional lattice along the vertical direction, resulting in a weak confinement along that direction and therefore weak correlations.

This equation was evolved in imaginary time to find the (localised) ground state for $\alpha = 2$, shown in Fig. 1b and in Extended Data Fig. 2 in log-scale. For the dynamical simulations of Figs. 3a and 3b, it was instead evolved in real time with a given ramp $V_0(t)$ from a uniform initial wavefunction.

The ramp times $\tau_{99\%}$ in Fig. 1d were fitted with:

$$y = \frac{a}{(V_{\text{loc}} - V_0)^b}, \quad \text{with} \quad \begin{array}{|c|c|c|} \hline & \text{value} & \text{error} \\ \hline a & 0.05 & 0.04 \\ \hline V_{\text{loc}} & 1.80 & 0.03 \\ \hline b & 3.15 & 0.80 \\ \hline \end{array} \quad (11)$$

which provided an estimate for $V_{\text{loc}}/E_{\text{rec}} = 1.80(3)$, shown as the grey bar.

For the inset in Fig. 4, the simulation solved for the ground state of the lattice of equation (10) in the presence of twisted boundary conditions [31], where the phase of the wavefunction is required to

differ by a small angle θ between opposite boundaries of the simulation region. A wavefunction localised at the origin is unaffected by such twist, as its magnitude at the boundary vanishes: the ground state energy of the localised phase is hence independent of the twist. A delocalised wavefunction, in contrast, displays a phase difference θ over the system size L , corresponding to a phase velocity $v \propto \theta/L$ and an associated additional kinetic energy. The sensitivity of the ground state energy between the untwisted and twisted systems ($\Delta E_g/\theta^2$) is directly proportional to the superfluid stiffness or superfluid fraction ψ_{SF} and is plotted in the inset of Fig. 4 as a function of lattice depth. At the localisation transition, the superfluid fraction vanishes.

To quantify the strength of the interactions, we consider the spatially averaged interaction energy per atom in a 3D box of size L :

$$E_{\text{int}} = \frac{1}{L^3} \int \frac{4\pi\hbar^2 a}{m} n(\mathbf{r}) d^3\mathbf{r}, \quad (12)$$

where $n(\mathbf{r})$ is the 3D density of the system. Assuming a system with atom number N that is translationally invariant in z , the simulated wavefunction ψ is normalised such that $\int |\psi|^2 d^3\mathbf{r} = L \int |\psi|^2 dx dy = \eta L$, where we defined $\eta = N/L$. This leads to:

$$E_{\text{int}} = \frac{1}{L^2} \frac{4\pi\hbar^2 a}{m} \eta, \quad (13)$$

and substituting in $E_{\text{rec}} = \hbar^2 k^2 / (2m)$ gives

$$E_{\text{int}} = 8\pi a \frac{\eta}{k^2 L^2} E_{\text{rec}}. \quad (14)$$

For the red curve in the inset of Fig. 4, a value of $a\eta = 0.3$ was used in a simulation volume of size $kL = 14\pi$, which corresponds to $E_{\text{int}} = 0.004 E_{\text{rec}}$. We checked that performing the simulation in a volume of size $kL = 64\pi$ while preserving E_{int} does not qualitatively affect the results.

Inverse Participation Ratio in momentum space (IPR_k)

A quantum state may be expressed in any complete orthonormal basis, for instance in the Wannier $|w_i\rangle$ or in the plane wave $|\phi_j\rangle$ bases:

$$|\Psi\rangle = \sum_i \psi_i |w_i\rangle = \sum_j \tilde{\psi}_j |\phi_j\rangle. \quad (15)$$

The Inverse Participation Ratio in momentum space IPR_k is defined as

$$\text{IPR}_k = \sum_j |\tilde{\psi}_j|^4, \quad (16)$$

and measures how many plane waves contribute to a given state. A large and finite IPR_k corresponds to the situation where only a handful of plane waves are of relevance — a large IPR is equivalent to a small participation ratio (PR), meaning a small ratio of participating states to available states. Normalisation imposes $\sum_i |\tilde{\psi}_i|^2 = 1$, and hence $\sum_i |\tilde{\psi}_i|^4 \leq 1$. The equality is only satisfied when the state consists of only *one* basis function, i.e. for a single plane wave. A state that is localised in real space, on the other hand, necessarily comprises an infinite number of plane waves and hence will have a vanishing IPR_k .

For periodic lattices, the single-particle eigenstates are always extended Bloch waves with a finite IPR_k , which approaches zero only asymptotically with lattice depth. The eightfold quasicrystalline lattice, in contrast, displays the sharp transition shown in Fig. 1e, signalling the localisation transition.

The following table provides a summary for the ground state IPR in real (IPR_x) and momentum (IPR_k) space characterising the delocalised (extended) and localised phases, highlighting the opposite behaviours:

		delocalised in x (localised in k)	localised in x (delocalised in k)
IPR_x	$\sum_i \psi_i ^4$	$\rightarrow 0$ (thermo. limit)	finite (1, Wannier functions)
IPR_k	$\sum_j \tilde{\psi}_j ^4$	finite (1, no lattice)	$\rightarrow 0$ (thermo. limit)

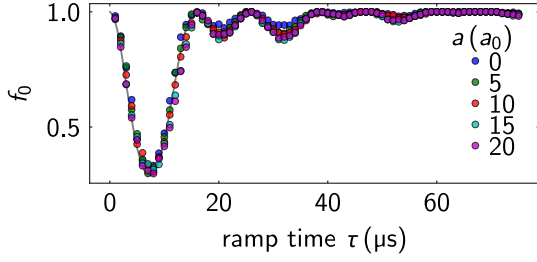
The IPR_k of the first few tens of low-lying eigenstates was also computed and exhibited the same qualitative behaviour as the ground state. The red curve in Fig. 1e was obtained by extrapolating the blue curves to the $n \rightarrow \infty$ limit — see equation (6). To this end we plotted the computed data for each lattice depth against $1/n$ and extracted the intercept of a fitted straight line.

Interacting data

The interaction strength was varied by employing the Feshbach resonance at 402.70(3) G of the $|1, 1\rangle$ state in ^{39}K [24].

We note that the maximum recovery of $f_0 \approx 0.9$ at $\tau \approx 30 \mu\text{s}$ (turquoise star in Fig. 3a) for $V_0 = 2.4 E_{\text{rec}}$ is independent of the interaction strength in the investigated range: the chemical potential at $a = 200 a_0$ in our harmonic trap is $\mu/h \approx 742 \pm 84 \text{ Hz}$. This corresponds to an interaction timescale $\sim 1.5 \text{ ms}$, which is large compared to the $\tau \approx 30 \mu\text{s}$ recovery time.

This is additionally illustrated in Extended Data Fig. 3, where the recovered zero-momentum fraction in the square lattice showed no change around



Extended Data Fig. 3 | Absence of interaction effects on square lattice ramps. The zero-momentum fraction f_0 is fully recovered for square lattices even for moderate repulsive interaction strengths, quantified by the scattering length a . Here, $V_0 = 7 E_{\text{rec}}$. The solid line is the same numerical solution to the single-particle Schrödinger equation shown in Fig. 2.

$\tau \approx 30 \mu\text{s}$ for small interactions (up to $a = 20 a_0$).

The recovered zero-momentum fractions at $\tau =$

$250 \mu\text{s}$ shown in Fig. 4 in the main text are therefore sufficient to determine the slope of the whole curve, which we use as an indicator of localisation (as shown in Fig. 3).

The chemical potential was calculated using the following expression valid within the Thomas-Fermi approximation [32]:

$$\mu = \frac{\hbar\bar{\omega}}{2} \left(\frac{15Na}{\bar{a}_{\text{ho}}} \right)^{2/5}, \quad (17)$$

where a is the scattering length, $\bar{\omega}$ the geometric mean of the dipole trap frequencies, N the atom number and $\bar{a}_{\text{ho}} = \sqrt{\hbar/m\bar{\omega}}$ the mean harmonic oscillator length.

The data in Fig. 4 is fitted phenomenologically with an error function:

$$a \cdot \text{Erf}[b(\mu - c)] + d, \quad (18)$$

	value	error
a	0.40	0.01
b	5.72×10^{-3}	2.9×10^{-4}
c	290.0	5.7
d	0.58	0.01